buildings

MDPI

Article

Research on the Preparation and Mechanical Properties of Solidified 3D Printed Concrete Materials

Yuhang Shen [1], Li Lin [1,*], Shengjie Wei [1], Jie Yan [1] and Tianli Xu [2,*]

[1] School of Architecture and Civil Engineering, Harbin University of Science and Technology, Harbin 150080, China
[2] School of Civil Engineering, Harbin Institute of Technology, Harbin 150090, China
* Correspondence: linli0119@163.com (L.L.); 19b933053@stu.hit.edu.cn (T.X.)

Abstract: Three-dimensional (3D) printing is an innovative manufacturing process based on 3D digital models that involves layer-by-layer addition of materials. In recent years, 3D printing has made good progress in the field of construction, thereby leading to more stringent requirements for materials. In this study, we first compare different equipment and materials used for 3D printing concrete. Subsequently, the mix ratio of extruded and cured 3D printed concrete is studied by using flow and slump as the main evaluation indexes. Through a universal test, the influence of different dosages of water reducer, retarder, and latex powder on the performance of 3D printed concrete (compression resistance strength) is studied. Furthermore, the optimum mix ratio for fiber reinforced concrete is determined, based on which axial pull-out, axial compression, and three-point bending tests are performed to elucidate the peak compressive strength, load–displacement curve, and mechanical properties of 3D printed concrete. By employing the ABAQUS finite element software, the shaft pulling force and axial compression of 3D printed concrete are simulated and analyzed to determine the parameters influencing the bonding performance of different 3D printed concrete layers. Moreover, the influence of water reducer and sand–glue ratio is observed to be greater than that of water gel ratio and sodium gluconate. The testing results showed that the mechanical strength of 3D printed concrete is lower than that of poured concrete. Meanwhile, bending and compressive strengths of 3D printed concrete and poured concrete are quite different.

Keywords: concrete; 3D printing; mix ratio; mechanical properties; numerical simulation

Citation: Shen, Y.; Lin, L.; Wei, S.; Yan, J.; Xu, T. Research on the Preparation and Mechanical Properties of Solidified 3D Printed Concrete Materials. *Buildings* **2022**, *12*, 2264. https://doi.org/10.3390/buildings12122264

Academic Editor: Abdelhafid Khelidj

Received: 17 November 2022
Accepted: 14 December 2022
Published: 19 December 2022

1. Introduction

Three-dimensional (3D) printing is a manufacturing process based on 3D digital models that involves layer-by-layer addition of materials [1,2]. This technology has the potential to effectively solve the problems associated with traditional building construction such as lengthy construction periods, low efficiency, wastage of manpower, and material resources, environmental pollution, and the difficulty to shape complex components. However, 3D printing has not been adequately developed for application in building construction; the theoretical research on printing material is lacking, and the influence of admixtures on the mechanical properties of 3D printed concrete needs further research [3]. Distinct from the traditional concrete preparation process, 3D printing of concrete is essentially a pouring process. A predetermined shape is printed by using the machine settings, and its height [4] can be controlled by altering the thickness of the print and number of layers. Related literature has also reported the instable performance of 3D printed concrete by changing the mix ratio of 3D printed concrete to alter its mechanical properties. The researchers at Loughborough University [5] developed a high-performance fiber-enhanced 3D printed concrete with fine aggregates, explored the admixture ratio, and identified factors influencing its performance. They designed multiple sets of concrete materials that were suitable for the 3D printing process and comprised different mix ratios to print large-scale free-form components, evaluate the feasibility of the concrete for the 3D printer, and determine the most optimum mix ratio of the concrete; they also identified parameters most optimum for printing, namely: a gel ratio of 1.5, a water–glue ratio of 0.26, a fly ash [6] proportion of 20%, a silica ash proportion of 10%, a polypropylene fiber content of 1.2 kg/m^3 [7], a water-reducing agent proportion of 1%, and a retarder proportion of 0.5%. Based on the optimal fit ratio, the opening time and mechanical properties of 3D printed concrete have also been studied. The opening time is controlled at 100 min and the compressive strength of the concrete exceeds the preset target, reaching 110 MPa at 28 d and 125 MPa at 56 d. Overall, the 3D printed concrete prepared at Loughborough University meets the performance requirements of 3D printed high-performance fiber reinforced concrete, and no collapse or tilt occurs.

In addition to the admixture ratio, some experts and practitioners have also studied the nozzle shape, printing rate, and object complexity [8], while testing the compression and tension strength of concrete. Furthermore, compression strength, bending strength, and other mechanical properties of the 3D printed specimen are also affected by the printing direction; therefore, these specimens exhibit anisotropy. Moreover, the printing time interval [9] has different effects on the interlayer strength, compressive strength, and flexural strength of the 3D printed concrete in different directions. Printing times of 10, 20, and 30 min reveal that the compression and bending strengths of 3D printed concrete are related to the surface water content [10] at the interlayer interface; therefore, increasing the interlayer delay time augments its strength. The compressive strength in the vertical direction lies between the compressive strength observed in other directions, regardless of the delay time.

Theoretically, mechanical properties of 3D printed mortar cannot be similar to those of traditional cast-in-place concrete. In fact, loading results in different directions exhibit anisotropy in 3D printed concrete. Feng et al. [11] used gypsum as the printing gel material for mechanical testing. They concluded that when loading in the X, Y, and Z directions, the damage form of the printing specimen is similar; although there are hourglass cracks on the left and right sides, the compressive strength along the X direction (printer head movement) and the elastic modulus are the largest.

There are various standardized methods and specifications for studying the mechanical properties of conventional concrete; however, their applicability to mortar strength testing remains uncertain. In general, the current test methods developed for concrete differ in terms of the sample form and size, mix ratio, material, time, and direction of the nozzle device. Adding fiber material can also enhance the mechanical properties of 3D printed concrete by increasing the compactness. Its anisotropy changes significantly with an increase in the fiber content. With the help of high-precision computed tomography scanning, Yanfeng et al. [12] have studied the mechanical characteristics of 3D printed concrete based on fine structural characteristics such as concrete interface area and pore defect distribution. The test results show that the initiation and expansion of cracks tend to occur due to the existence of many internal pores, voids, and weak interlayer surfaces produced in the construction process, which is the direct cause of the mechanical anisotropy of cracks.

This paper elucidates the mechanical properties of 3D printed concrete with two main objectives:

1. Determining the influence of different admixtures on the performance of concrete through single-factor experiments: an orthogonal combination test [13] has been used to analyze the interaction between different factors to determine the basic mix ratio of printed concrete. According to the requirements of the 3D printing process, fiber optimization is conducted, and the mix ratio of fiber-reinforced concrete is determined.
2. Analyzing the difference in the failure mode and ultimate compressive strength of the 3D printed concrete under different load directions: This objective is achieved by conducting the axial pull-out [14], axial compression [15], and three-point bending tests [16]. By numerically simulating a cohesion [17], mechanical properties of the

3D printed concrete are analyzed. Consequently, a 3D printed beam is developed, the mechanical properties of this beam are analyzed, and the feasibility of different printing paths [18] is explored. Overall, the study findings provide a theoretical basis for elucidating the mechanical properties of 3D printed concrete.

2. Materials and Methods

2.1. Introduction of Equipment

The equipment used in this study [19] consists of four modules: control system, motion system, extrusion system, and data processing system. The control system provides the commands and has the following functions: microprocessor function, external input function, G code interpretation function, axis linkage function, mechanical signal processing function, human–computer interaction interface, etc. The motion system is used to realize three-dimensional movement of the nozzle, which is applied to actual printing. The extrusion system consists of a pumping device, feeding pipeline, mixer, and nozzle [20], as shown in Figure 1.

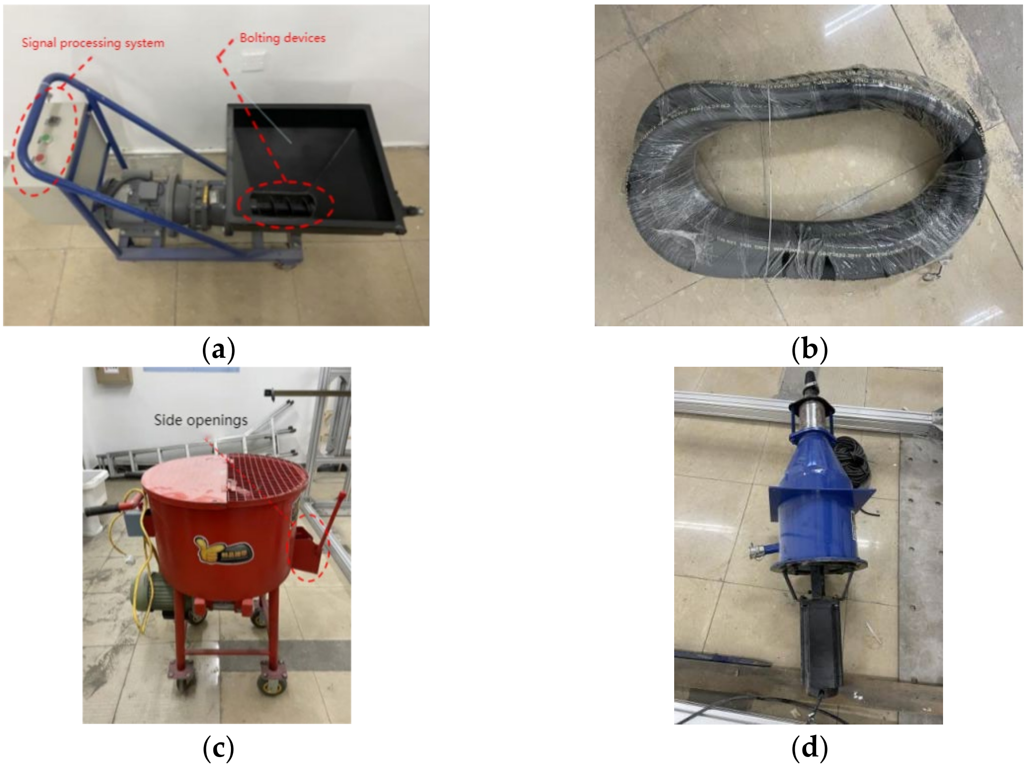

Figure 1. Components of the extrusion system: (**a**) pumping device; (**b**) feed pipes; (**c**) mixer; (**d**) print nozzles.

The printing process employed here can be divided into three stages: data preparation, concrete preparation, and model printing. In the data preparation stage, the component model is drawn using BIM, after which the files are exported in the STL format. Next, the model is sliced up to the design layer depth, and then the printing path required to generate the G code file is determined. Subsequently, the concrete mixture is added to the pumping device, and the drive control system smoothly transports the mortar through the pump pipe-nozzle. The dense concrete filament is printed first, which ensures that the structural components are built layer by layer. The printing process is shown in Figure 2.

The admixtures used in this experiment, such as water reducer [21], glue powder, and retarder [22,23], improve the tension strength of the component and reduce the number of microcracks. The low activity of fly ash [24] in additives reduced the initial concrete strength. To increase the activity of fly ash in concrete, CH powder and fly ash can be mixed together with a 6 mm basalt fiber [25] and 15 mm fiberglass [26]. Concrete curing temperature is 20 ± 2 °C, while humidity is not less than 95%. Maintenance is performed every 7 d and 28 d.

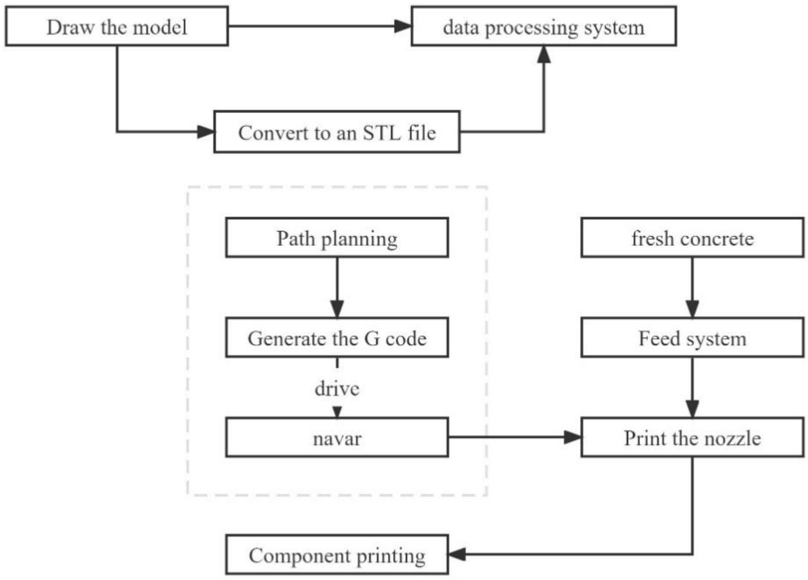

Figure 2. Workflow of the 3D printing process.

3D printing of concrete considers extrudability, constructability, and ease of implementation as the performance indices. The cement used here (RSC42.5 grade fast hard-sulfur aluminate cement) [27] is produced by Wuxi Chengde Yue Building Materials Co., LTD. The main performance indicators are shown in Table 1. The aggregate used in this study exhibits a quartz sand content of 30–40%, and it has been provided by the Tai Xuefeng, Chengdu, Sichuan province. Its main component is SiO_2, and the corresponding performance indices are shown in Table 2. The secondary fly ash and CH powder selected in the test have been provided by Hengyuan New Material Co., Ltd.; their performance indicators are shown in Tables 3 and 4, respectively.

Table 1. Performance indices of sulphoaluminate cement.

Compression Strength (MPa)		Rupture Strength (MPa)		Specific Area	Setting Time	
3 d	28 d	3 d	28 d	(m^2/kg)	Start	Stop
21.5	52.5	6.8	12.4	542	10	25

Table 2. Performance indices of quartz sand.

Material	Burning Reduces Quality (%)	Water Absorption (%)	Hardness	Density (kg/m^3)
Quartz sand	0.03	1.3	7.5	2640

Table 3. Physical performance indices of fly ash.

Material	Sulfur Anhydride (%)	Burning Vector (%)	Stacking Density (g/cm)	Density (g/cm^3)	Moisture Content (%)	Fineness (%)
Fly ash	2.1	2.8	1.12	2.55	0.125	16

2.2. Test Methods

2.2.1. Orthogonal Test Design

An orthogonal test has been conducted by selecting the representative test points and analyzing the results of the typical test to identify the most optimum production process. The materials used in this study are 300 g of cement, 100 g of mineral powder [28], 100 g of fly ash, 1 g of concrete foaming agent, and 10 g of latex powder. The L16 (44) orthogonal table has been used for testing, where 16, 4, and 4 represent the number of trials, levels, and factors, respectively. Table 5 shows the value of different influencing factors at different levels, while Table 6 represents the orthogonal table. The additive percentage has been measured as the mass percent.

Table 4. Performance indices of CH mineral powder.

Material	Specific Area (m^2/kg)	Density (kg/m^3)	Burning Vector (%)	Flow Ratio (%)	Activity Index for 7 Days (%)	Activity Index for 28 Days (%)
CH mineral	422	2.86	1.3	75	105	114

Table 5. Value of each influencing factor at different levels.

Level	Influencing Factors			
	Water to Glue Ratio/1	Sand to Glue Ratio/1	Water Reducer/%	Retarder/%
1	0.26	0.7	0.05	0.1
2	0.28	0.9	0.15	0.2
3	0.30	1.1	0.25	0.3
4	0.32	1.3	0.35	0.4

Table 6. Result of the orthogonal test.

Test Number	Influencing Factors			
	Water to Glue Ratio	Sand to Glue Ratio	Water Reducer/%	Retarder/%
ZJ-1	0.26	0.7	0.05	0.1
ZJ-2	0.26	0.9	0.15	0.2
ZJ-3	0.26	1.1	0.25	0.3
ZJ-4	0.26	1.3	0.35	0.4
ZJ-5	0.28	0.7	0.15	0.3
ZJ-6	0.28	0.9	0.05	0.4
ZJ-7	0.28	1.1	0.35	0.1
ZJ-8	0.28	1.3	0.25	0.2
ZJ-9	0.30	0.7	0.25	0.4
ZJ-10	0.30	0.9	0.35	0.3
ZJ-11	0.30	1.1	0.05	0.2
ZJ-12	0.30	1.3	0.15	0.1
ZJ-13	0.32	0.7	0.35	0.2
ZJ-14	0.32	0.9	0.25	0.1
ZJ-15	0.32	1.1	0.15	0.4
ZJ-16	0.32	1.3	0.05	0.3

2.2.2. Single-Axial Test

A uniaxial test [29], which is divided into a tension test and compression test, has been conducted using a 200 kN WDW testing machine with a load-control loading mode; the loading rate is 0.02 kN/s. The specimen preparation process is shown in Figure 3.

(**a**) (**b**) (**c**) (**d**)

Figure 3. Preparation process of the 3D printed axial tension specimen. (**a**) Specimen printing; (**b**) Specimen is printed and formed; (**c**) Specimen cutting; (**d**) Specimen preservation.

3. Results and Discussion

3.1. Analyses of Orthogonal Test Results

The extreme difference analysis method [30] has been used in this study to elucidate the orthogonal test results, with flow and slump being the primary evaluation indexes [31] while compressive strength and bending strength [32] are the secondary evaluation indexes. The test results are shown in Table 7.

Table 7. Orthogonal test results.

Test Number	Flow/mm	Slump/mm	Compressive Strength at 3rd Day/MPa	Compressive Strength at 28th Day/MPa	Flexural Strength at 3rd Day/MPa	Flexural Strength at 28th Day/MPa
ZJ-1	170	160	33.3	56.1	6.6	11.9
ZJ-2	155	145	20.1	48.3	5.4	10.1
ZJ-3	155	110	21.8	49.4	4.9	8.1
ZJ-4	145	70	17.4	41.2	4.4	8.5
ZJ-5	218	230	16.9	46.7	5.1	6.1
ZJ-6	175	180	23.6	51.5	6.1	10.4
ZJ-7	155	160	18.0	43.4	4.5	9.5
ZJ-8	145	70	23.3	50.0	6.0	9.1
ZJ-9	248	270	25.2	51.6	6.5	9.2
ZJ-10	215	230	21.3	48.7	5.7	11.2
ZJ-11	168	175	22.7	49.7	6.0	9.5
ZJ-12	145	85	22.3	48.4	5.8	8.9
ZJ-13	280	290	22.8	48.2	5.6	9.1
ZJ-14	235	265	18.3	44.7	5.2	8.0
ZJ-15	180	220	19.6	47.9	5.4	7.3
ZJ-16	160	160	22.5	49.7	5.9	10.1

3.2. Analysis of the Extreme Difference between Flow and Slump

According to the test results in Table 4, the influence of different factors on the flow and slump of concrete is analyzed. Results of the analysis are shown in Tables 8 and 9.

The extreme difference values exhibit the following relationship for both slump and flow: sand–glue ratio > water gel ratio > water reducing agent > sodium gluconate [33]. When the permeability ratio [34] of sand glue ratio is 0.8 and 1.1, flow and slump do not meet the requirements of 3D printing and should not be considered. Furthermore, the mixing amount should be controlled between 0.9 and 1.1.

Based on Figure 4a, the water–glue ratio has a contrasting effect on flow and slump when compared to the effect that the sand–glue ratio has. With an increase in the water–glue ratio, there is a flow and slump increase in a linear trend. When the water–glue ratio is 0.28, the flow degree is 173.2 mm and the slump degree is 160.0 mm, which meets the 3D printing requirements; meanwhile, the water–glue ratio is determined to be 0.28.

Table 8. Influence of various factors on flow.

Numbering	Flow/mm			
	Water to Glue	Sand to Glue Ratio	Water Reducer	Sodium Gluconate
K_1	156.3	229.0	168.2	176.3
K_2	173.2	195.0	174.5	187.0
K_3	194.0	164.5	195.7	187.0
K_4	213.8	148.8	198.8	187.0
Range R	57.50	80.20	30.50	10.70

Table 9. Influence of various factors on slump.

Numbering	Slump/mm			
	Water to Glue	Sand to Glue Ratio	Water Reducer	Sodium Gluconate
K_1	121.25	237.50	168.75	167.50
K_2	160.00	205.00	170.00	170.00
K_3	190.00	166.25	178.75	182.50
K_4	233.75	96.25	187.50	185.00
Range R	112.50	141.25	18.75	17.50

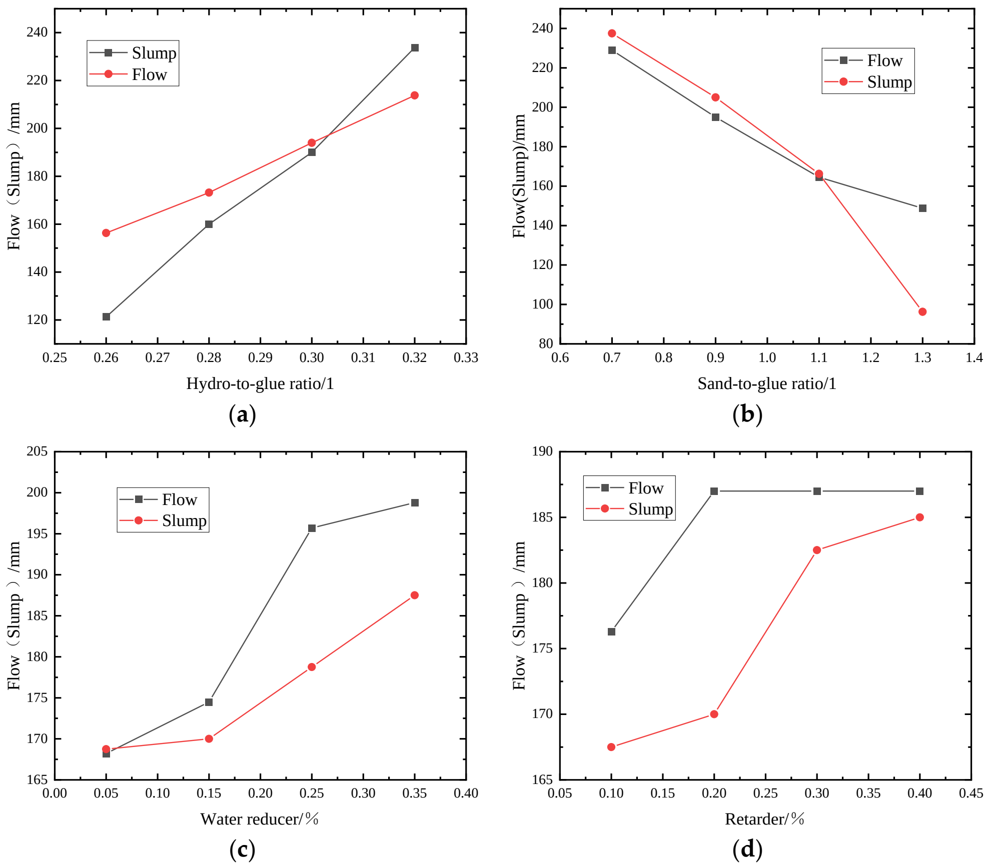

Figure 4. Influence of various factors on flow and slump. (**a**) Water-to-glue ratio; (**b**) Sand-to-glue ratio; (**c**) Water reducer; (**d**) Sodium gluconate.

Figure 4c,d indicate that the flow rate and slump slowly increase as the contents of the water reducer [35] and sodium gluconate increase. When the sodium gluconate content exceeded 0.2%, there was no effect on the flow rate, while the slump was increased by 0.20% to 0.30%. Meanwhile, the sodium gluconate content is 0.23%, and the water reducer content is controlled to range between 0.15% and 0.23% according to the printing requirements; the specific dose is dependent on the simulated intensity.

3.3. Differential Analyses of Compressive Strength

The extreme differential analysis [36] is used in this study to analyze the influence of each factor on the compressive strength of concrete at day 3 and 28, and the analysis results are shown in Tables 10 and 11.

Table 10. Influence of various factors on the compressive strength at 3 d.

Numbering	Compressive Strength at 3 d/MPa			
	Water to Glue Ratio	Sand to Glue Ratio	Water Reducer	Sodium Gluconate
K_1	23.40	24.55	25.52	22.97
K_2	20.45	21.07	19.52	22.48
K_3	22.88	20.52	22.15	20.63
K_4	20.80	21.38	19.88	21.45
Range R	2.95	4.02	5.65	2.35

Table 11. Influence of various factors on the compressive strength at 28 d.

Numbering	Compressive Strength at 28 d/MPa			
	Water to Glue Ratio	Sand to Glue Ratio	Water Reducer	Sodium Gluconate
K_1	48.75	50.65	51.75	50.42
K_2	50.17	48.30	47.83	49.05
K_3	49.60	49.88	48.92	48.63
K_4	47.63	47.33	47.65	48.05
Range R	2.55	3.33	4.10	2.37

The extreme difference values exhibit the following relationship for compressive strength at both 3rd and 28th day: water reducing agent > sand–glue ratio > water–gel ratio > sodium gluconate. The key to control compressive strength is to alter the contents of water reducer and gel ratio.

3.4. Extreme Difference Analysis of Bending Resistance Strength

According to the test results in Table 6, the influence of each factor on the bending strength of concrete at 3 d/28 d was analyzed. Results of the analysis are shown in Tables 12 and 13.

Table 12. Influence of various factors on flexural strength after 3 d.

Numbering	Flexural Strength at 3 d/MPa			
	Water to Glue Ratio	Sand to Glue Ratio	Water Reducer	Sodium Gluconate
K_1	5.325	5.950	6.150	5.525
K_2	5.425	5.600	5.425	5.750
K_3	6.000	5.200	5.650	5.400
K_4	5.525	5.525	5.050	5.600
Range R	0.675	0.750	1.110	0.350

Table 13. Influence of various factors on flexural strength after 28 d.

Numbering	Flexural Strength at 28 d/MPa			
	Water to Glue ratio	Sand to Glue Ratio	Water Reducer	Sodium Gluconate
K_1	9.650	9.075	10.475	9.575
K_2	8.775	9.925	8.100	9.450
K_3	9.700	8.600	8.600	8.875
K_4	8.625	9.150	9.575	8.850
Range R	1.075	1.325	2.375	0.725

The extreme difference values exhibit the following relationship for flexural strength at both 3rd and 28th day: water reducing agent > sand–glue ratio > water–gel ratio > sodium gluconate. As shown in Figure 5, sand gel ratio of 1.1 and retarder content of 0.2% are reasonable.

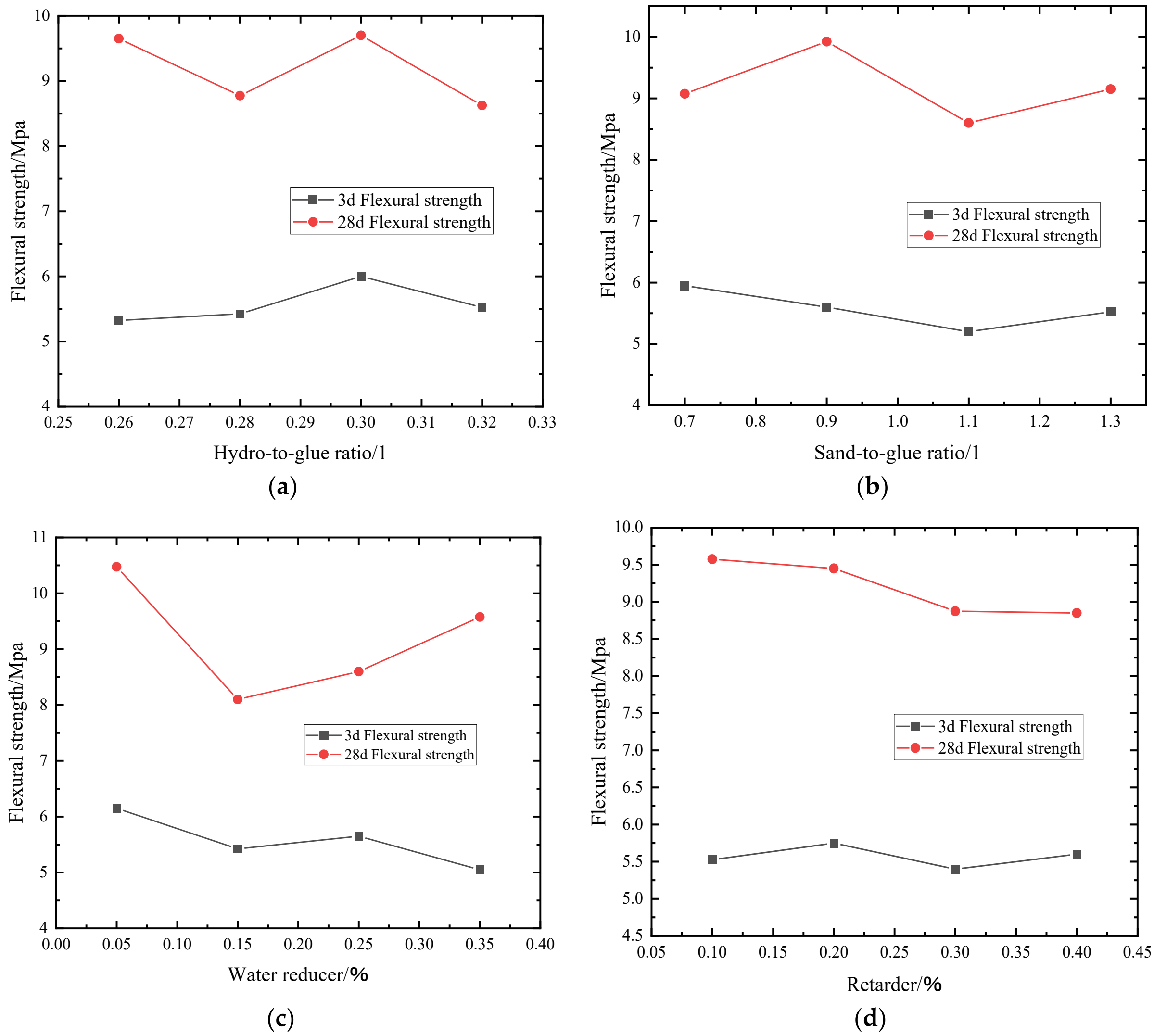

Figure 5. Influence of various factors on the flexural strength at 3 d/28 d. (**a**) Water-to-glue ratio; (**b**) Sand-to-glue ratio; (**c**) Water reducer; (**d**) Retarder.

In summary, based on the requirements of the 3D printed concrete with regard to flow, slump, and setting or hardening time, the mix ratio of 3D printed concrete is determined (Table 14).

Table 14. Mix ratios of 3D printed concrete.

Water-to-Glue Ratio	Sand-to-Glue Ratio	Cement	Fly Ash	Mineral Powder	Water Reducer	Retarder	Latex Powder	Defoamer
/%	/%	/%	/%	/%	/%	/%	/%	/%
0.29	**1**	**60**	**20**	**20**	**0.20**	**0.23**	**2**	**0.2**

3.5. Uniaxial Test Results and Discussion

3.5.1. Tension Test

Cracks are produced in a small area of the middle section during the dog bone test, where the nature of damage is brittle and the axial tension ceases. The peak load of each test piece is recorded to determine the mechanical properties under axial pull. Meanwhile, the cross-sectional area and tension strength of different specimens are calculated, as shown in Table 15.

Table 15. Results of the axial tension test.

Category	Specimen Number	Peak Load (kN)	Cross-Sectional Area (mm^2)	Tensionon Strength (Mpa)	Average Strength (Mpa)
Specimen printed horizontally	LH-1	0.365	19.5 × 28.9	1.33	1.41
	LH-2	0.412	18.9 × 30.7	1.51	
	LH-3	0.387	19.4 × 29.6	1.39	
Specimen printed vertically	LV-1	0.889	19.4 × 31.4	1.46	1.56
	LV-2	0.841	18.9 × 28.7	1.55	
	LV-3	0.978	19.8 × 29.4	1.68	
Poured specimen	LX-1	0.831	18.7 × 30.4	1.86	1.91
	LX-2	0.944	19.3 × 29.1	2.12	
	LX-3	0.721	19.1 × 29.2	1.75	

The load–displacement curves of the horizontally printed, vertically printed, and poured specimens are shown in Figure 6.

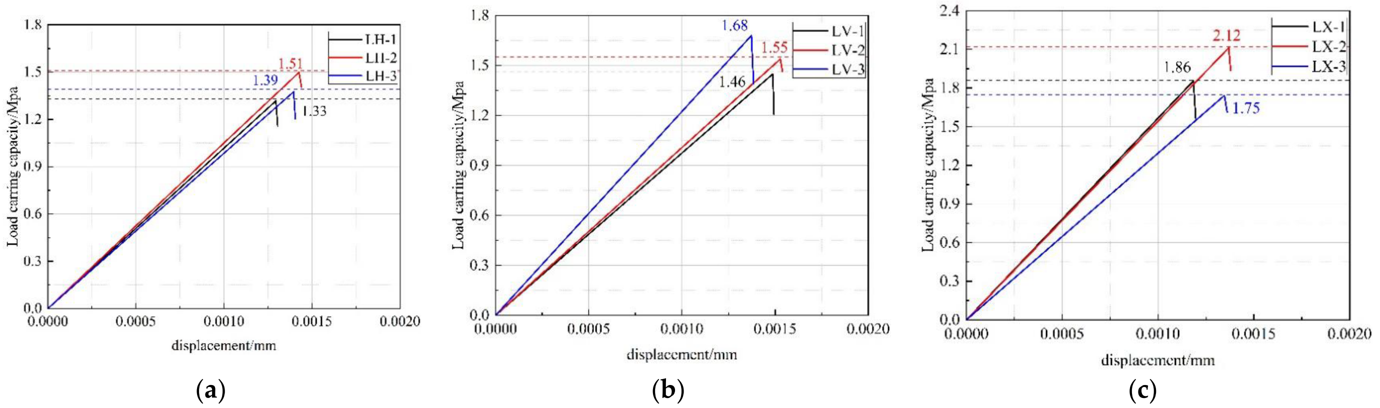

Figure 6. Load–displacement curves associated with the axial tension test. (**a**) Specimen printed horizontally; (**b**) Specimen printed vertically; (**c**) Poured specimens.

The average tension strength of the three specimens exhibits the following order: pouring specimen > vertically printed specimen > horizontally printed specimen. The average tension strength of the horizontally printed specimen and vertically printed specimen is 73.8% and 81.7%, respectively. The 3D printed specimen comprises strip concrete layers, which tend to be weak inside the specimen, resulting in reduced tension strength. Bonding modes of horizontally and vertically printed specimens tend to differ, and so does the bonding performance between any two layers. Since vertically printed specimens are formed under the action of gravity, their integrity is better than that of horizontally printed specimens. Meanwhile, horizontally printed specimens exhibit lower tension strength than that of vertically printed specimens [37].

3.5.2. Single-Axial Compression Test

Nine test specimens have been designed in this study, among which three sets of specimens are subjected to either the Z-axis, X-axis, or Y-axis loading. The Z-axis is perpendicular to the concrete layers, the X-axis is parallel to the concrete layers and oriented toward the printing direction, and Y-axis is parallel to the concrete layers and perpendicular to the X-axis. Three poured specimens have been set up as control groups. Peak load of each specimen is summarized in Table 16, and the cross-sectional areas of all specimens have been measured to accurately calculate their compressive strength.

Table 16. Results of axial compression testing.

Category	Specimen Number	Peak Load (KN)	Cross-Sectional Area (mm^2)	Compressive Strength (Mpa)	Average Strength (Mpa)
Z-axis loading	CZ1	73.23	39.2 × 40.7	45.9	43.5
	CZ2	64.94	38.3 × 41.7	40.7	
	CZ3	69.95	39.4 × 40.5	43.8	
X-axis loading	CX1	76.46	39.2 × 40.3	48.4	48.5
	CX2	79.75	38.9 × 39.5	51.9	
	CX3	73.38	39.8 × 40.7	45.3	
Y-axis loading	CY1	80.59	39.1 × 40.1	51.4	48.9
	CY2	73.66	38.4 × 40.9	46.9	
	CY3	77.37	38.8 × 41.2	48.4	
Poured specimens	C1	86.62	40.3 × 40.1	53.6	53.7
	C2	90.64	39.4 × 41.3	55.7	
	C3	84.32	39.8 × 40.9	51.8	

According to the test results, the load–displacement curve of each test group is drawn (Figure 7).

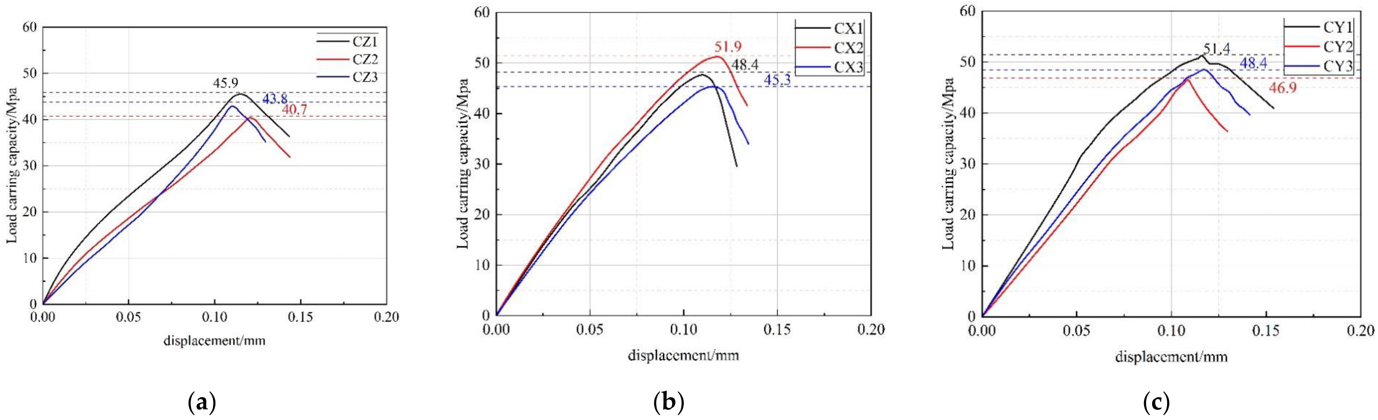

Figure 7. Load–displacement curves associated with the axial tension test. (**a**) CZ group specimens; (**b**) CX group specimens; (**c**) CY group specimens.

The compressive strength of samples loaded in Z-axis, X-axis, and Y-axis directions is 43.5 Mpa, 48.5 Mpa, and 48.9 Mpa, respectively. Meanwhile, that of the cast-in-place reinforced concrete is 53.7 Mpa. The compressive strengths in the direction of X and Y axes are similar, while being greater than that observed in the Z axis direction; therefore, anisotropy is evident. Due to the different bonding modes (extrusion bonding and stacking bonding) between the layers of 3D printed concrete, different printing directions, such as X and Y directions, the force is parallel to the printing layer during the compression test, and the complete printing layer makes the value measured in the direction of X and Y greater than the Z direction. Along with the weight and load of the upper print layer, concrete compaction and short column effect, therefore these results were observed.

4. Finite Element Simulation

There are few test blocks in this test, and due to the influence of laboratory temperature difference and humidity, the mechanical performance test of different batches of test blocks is different, which is not universal. According to the 3D printed concrete data measured in Chapter 3, the data show that the mechanical properties of the concrete optimized after the mixing ratio are close to those of C55 concrete. According to previous studies, concrete with similar strength generally has similar mechanical properties and change trend. Considering the uncertainty in the process of making and curing of concrete test block, the data may have large errors, which may lead to large error for finite element, and is not suitable for finite element [38], so C55 strength concrete is used to simulate the change trend of mechanical properties of concrete after optimized mix ratio. The finite element part adopts C55 concrete parameters (Table 17), and the finite element division of 3D printed concrete is considered a homogeneous material. This test is special, and the results of this simulation are only valid for the concrete mix ratio in this study.

Table 17. Concrete material parameters.

Density (kg/m^3)	Poisson's Ratio	Elastic Modulus (MPa)	Standard Value for Cube Compressive Strength (MPa)	Standard Value for TensionStrength (MPa)
2500	0.2	35500	35.5	2.74

The stress–strain relationship of concrete is indicated using Equations (1) and (2):

$$\sigma_c = (1 - d_c) E_0 \varepsilon_c \tag{1}$$

$$\sigma_t = (1 - d_t) E_0 \varepsilon_t \tag{2}$$

where σ_c is the uniaxial compressive stress, d_c represents the uniaxial compression damage evolution, E_0 is the elastic modulus, ε_c is the uniaxial compressive strain, σ_t is the uniaxial tension stress, d_t represents the uniaxial tension damage evolution, and ε_t is the uniaxial tension strain.

The plastic damage model represents the constitutive model of 3D printed concrete, whose stress and strain have been calculated using Equations (3) and (4). Meanwhile, the damage factors D_c and D_t are calculated using Equations (5) and (6):

$$\tilde{\varepsilon}_c^{pl} = \tilde{\varepsilon}_c^{in} - \frac{D_c}{(1 - D_c)} \frac{\sigma_c}{E_0} \tag{3}$$

$$\tilde{\varepsilon}_t^{pl} = \tilde{\varepsilon}_t^{ck} - \frac{D_t}{(1 - D_t)} \frac{\sigma_t}{E_0} \tag{4}$$

$$D_c = 1 - \sqrt{1 - d_c} \tag{5}$$

$$D_t = 1 - \sqrt{1 - d_t} \tag{6}$$

where $\tilde{\varepsilon}_c^{pl}$ is the equivalent plastic compressive strain, $\tilde{\varepsilon}_c^{in}$ is the inelastic compressive strain, D_c is the compression damage factor, σ_c is the concrete single-axis compressive stress, E_0 is the elastic modulus, ε_t is the uniaxial tension strain, $\tilde{\varepsilon}_t^{pl}$ is the equivalent plastic tension strain, $\widetilde{\varepsilon}_t^{ck}$ is the tension cracking strain, D_t is the tension damage factor, and σ_t is the single-axis tension stress.

The remaining parameters of the concrete plastic damage model are shown in Table 18.

Table 18. Other parameters of the plastic damage model.

Expansion Angle	Flow Potential Eccentricity	Ratio of Biaxial CompressiveStrength to Uniaxial Compressive Strength	K	Viscous Parameters
40	0.1	1.16	0.66667	0.005

4.1. Tension Simulation of Components

Mechanical properties of 3D printed concrete during shaft pulling are simulated using the ABAQUS finite element software. The Revit software is used to establish the concrete model [39], whose size parameters are the same as those of the specimen in Section 2.2. A full fixed constraint is applied to the bottom of the model, and the reference point is set at the top. The coupling instruction is used to couple the force on the specimen surface subjected to axial pulling with the reference point and apply an upward load to the point. The adhesion unit is placed between the disassembly layers; since it only 0.1 mm thick, it is negligible in size when compared to the Axle test model (Figure 8). The normal strength of the model Cohesive unit is 1.35 MPa and its tangential strength is 1.2 MPa. Convergence analysis of the finite element model mesh is conducted before geometric meshing, while 3.0 mm, 4.0 mm, 5.0 mm, 6.5 mm, and 8.0 mm are selected as the mesh sizes.

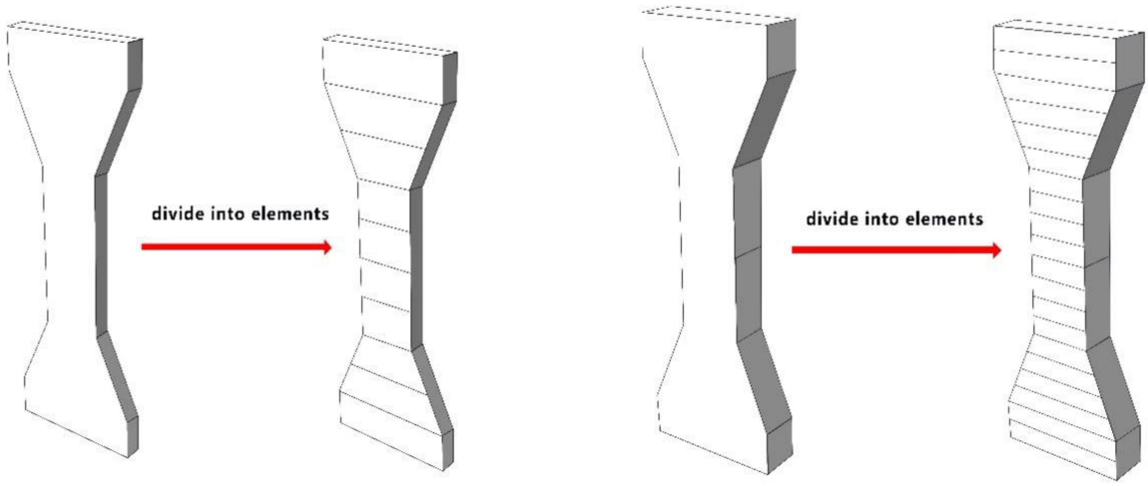

(**a**) (**b**)

Figure 8. Geometric division of the axial tension model. (**a**) Specimen is printed horizontally; (**b**) Specimen is printed vertically.

Considering the accuracy and calculation efficiency of the simulation results, a grid of size 4.0 mm is selected, and the calculation results are shown in Figure 9.

Numerical simulations show that the bond layer of 3D printed concrete breaks under vertical tension, which is consistent with the fracture pattern of the uniaxial tension test in Section 3.5. By calculating the reaction force at the reference point, the tension strength of the horizontally and vertically printed structures is determined to be 1.35 MPa and 1.48 MPa, respectively. The simulated and experimental results have been compared in Figure 10 and Table 19.

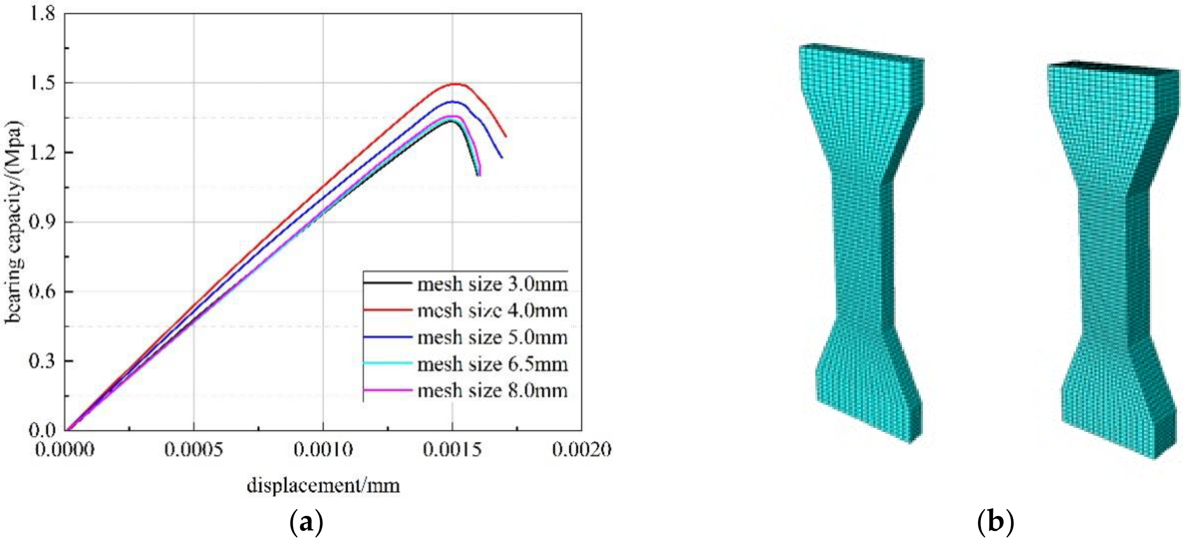

Figure 9. Analysis of grid convergence in the axial tension model. (**a**) Calculation results; (**b**) Axial tension model subjected to meshing.

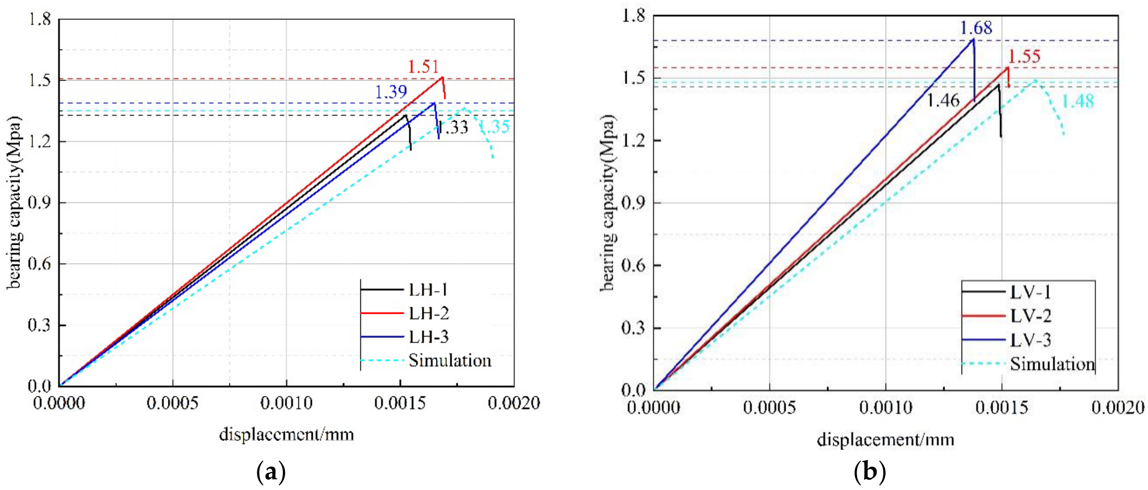

Figure 10. Load–displacement curves. (**a**) Horizontally printed specimen; (**b**) Vertically printed specimen.

Table 19. Comparative analysis of axial tension test and numerical simulation.

Testing Number	Strength (MPa)		Simulated Intensity (MPa)	Difference between the Experimental and Simulated Values (%)
	Experimental Values	Mean Values		
LH-1	1.33			
LH-2	1.51	1.41	1.35	4.4%
LH-3	1.39			
LH-4	1.46			
LH-5	1.55	1.56	1.48	5.4%
LH-6	1.68			

The average tension strength of horizontally printed specimens is 1.41 MPa, which is greater than the simulated value by 4.4%. Meanwhile, the average tension strength of vertically printed specimens (1.56 MPa) is greater than the simulated value by 5.4%. This may be due to the addition of glass fiber, it ensures that there is a closer bonding between the layer. Due to the effect of gravity in vertical printing, the tensile force is greater compared with horizontal printing, but due to the thin thickness of the component, the performance of vertical printing is slightly higher than that of horizontal printing, but it is not obvious. The gap in the two directions is only 1%, and this data is not necessarily general considering the errors in the test block preparation process. The test block printed in two directions is less than 6% wrong than the simulated value, which is acceptable. Therefore, the simulation can be used instead to analyze the change of its mechanical properties.

4.2. Axial Compression Simulation

The axial tension model is a 40 mm side-length cube. Based on the 3D-printing concrete process, the model is divided into four layers and two columns, and each layer of concrete is 10 mm thick and 20 mm wide (Figure 11). The Cohesive unit is set between the disassembly layers and is 0.1 mm thick; it exhibits a normal strength of 1.35 MPa and tangential strength of 1.2 MPa.

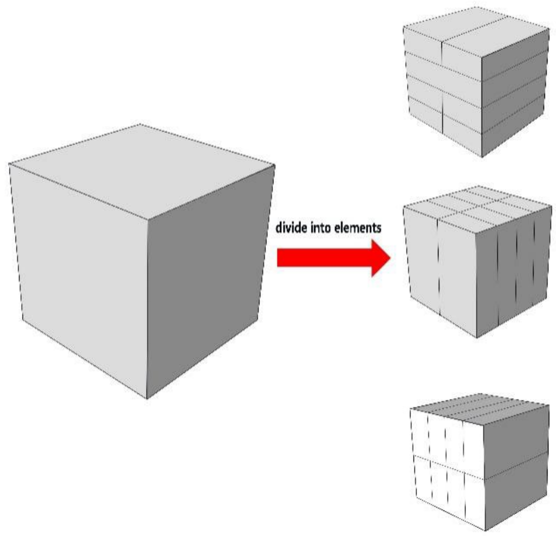

Figure 11. Geometric division of axial compression specimens.

4.2.1. Z-Axis Compression Simulation

Here, a grid of size 2.0 mm is selected. For finite element simulation of the axial pressure test, cloud maps depicting concrete compression damage, bonding unit damage, and Mises stress have been extracted from results, as shown in Figures 11 and 12.

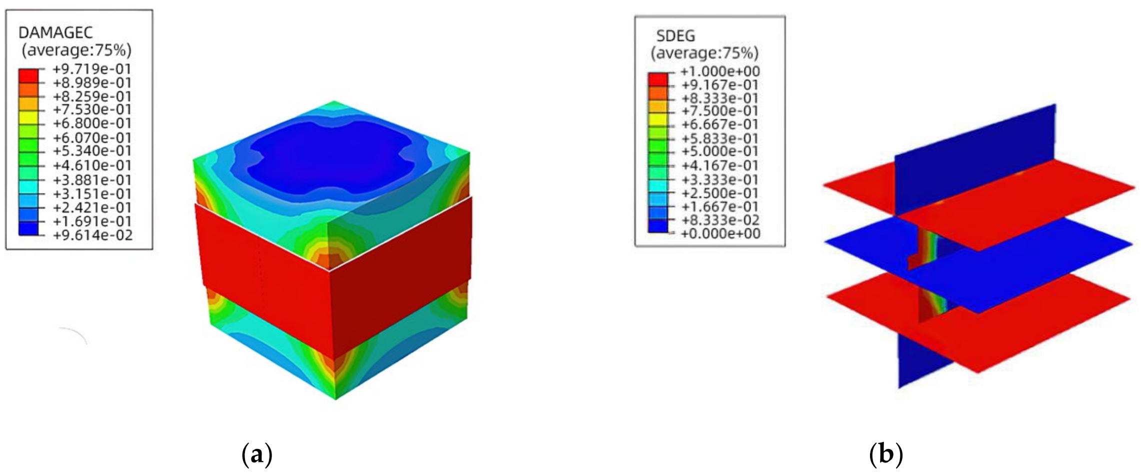

Figure 12. Damage cloud maps of specimen subjected to Z-axis loading compression. (**a**) Concrete compression damage; (**b**) Adhesive unit damage.

Figure 12 shows that compression damage is the highest (close to 1) and causes cracks in the specimen. Since downward cracks occurred in the vertical bonding layer, the cohesive unit was damaged, and the concrete cracked. The compression damage in the horizontal two-layer cohesion is l and some units fail at the edge of the vertical bonding unit, which is consistent with the cloud map depicting concrete compression damage.

Figure 13 shows that the maximum stress value of the specimen subjected to axial compression is 50.60 MPa, and the edges at the upper and lower ends and at the middle part of the specimen are large. Meanwhile, high stress is observed at the edge of both ends of the specimens, causing the concrete to break and fall off; vertical cracking is also observed in the middle parts. Overall, the simulation results are consistent with the experimental results.

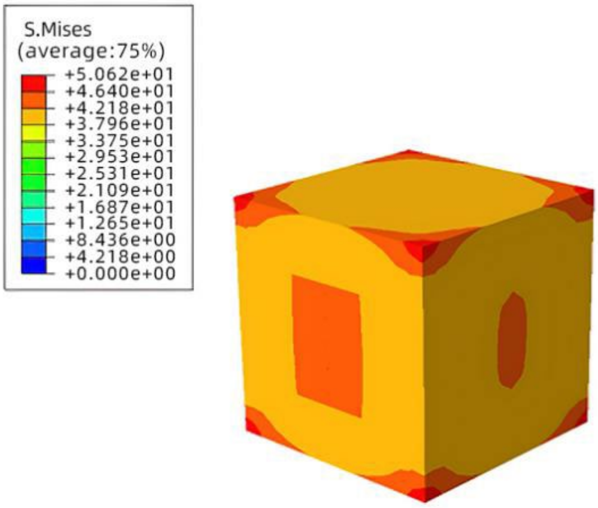

Figure 13. Stress cloud diagram of specimen subjected to Z-axis loading compression.

The load–displacement curves of specimens subjected to Z-axis loading compression are compared with the simulation results, as shown in Figure 14 and Table 20.

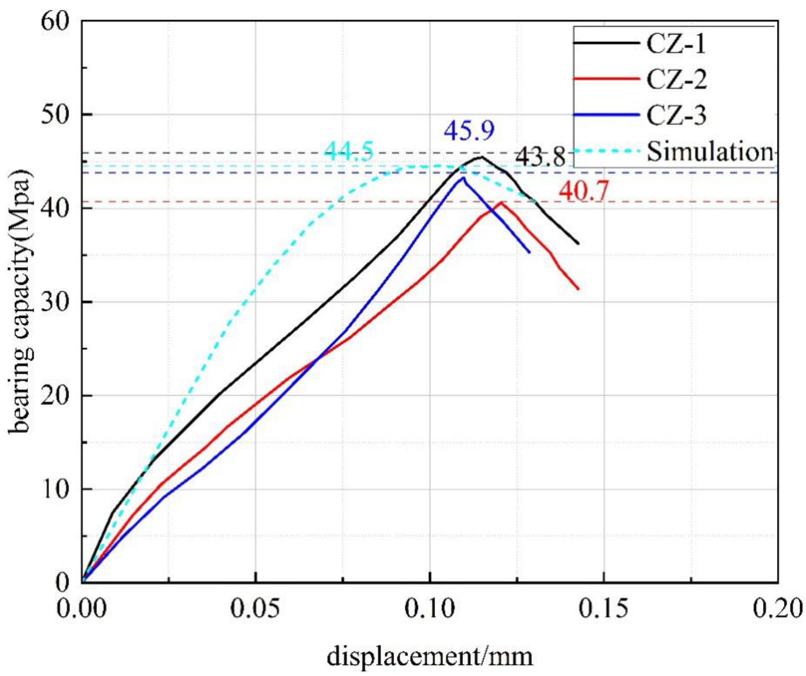

Figure 14. Load–displacement curves associated with the Z-axis compression test and corresponding numerical simulation.

Table 20. Comparative analysis of Z-axial compression testing and numerical simulation.

Specimen Numbering	Strength (MPa) Test Values	Experimental Average	Simulated Intensity (mpa)	The Ratio of the Test Value to the Simulated Value (%)
CZ1	45.9	43.5	44.5	97.8%
CZ2	40.7			
CZ3	43.8			

Table 20 shows the average of Z-axial compression strength of different specimens, as well as the simulated compression strength. According to the tensile test, the concrete performance of the optimized mix ratio should be slightly higher than that of C55 concrete, but the compression test value of Z axis is less than the simulated value, and it is 97.8% of the simulated value. This may be because in the preparation process of 3D printed concrete compression test block, often used by printing out the strip concrete and then cutting the test block. In this process, the edge of the test block receives downward pressure, and due to the influence of the printing layer first starting to solidify, it may lead to the weak bonding between the layers of the test block edge, and the performance can-not give full play in the compression test, and the fixed force is relatively small compared with the simulation.

4.2.2. X-Axis Compression Simulation

Cloud maps depicting concrete compression damage, bonding unit damage, and Mises stress caused by X-axis loading are shown in Figures 4–9.

Figure 15 shows that compression damage gradually weakened from the edge to the middle. The compression damage at the edge is close to 1, where the concrete layer suffers from crushing damage and cracks are formed. The concrete layer produced vertical cracks throughout the specimen, and compression damage at the two edges of the cohesion is close to 1. Overall, the bonding unit is damaged, and the concrete specimen is cracked, which is in accordance with the cloud map depicting concrete compression damage.

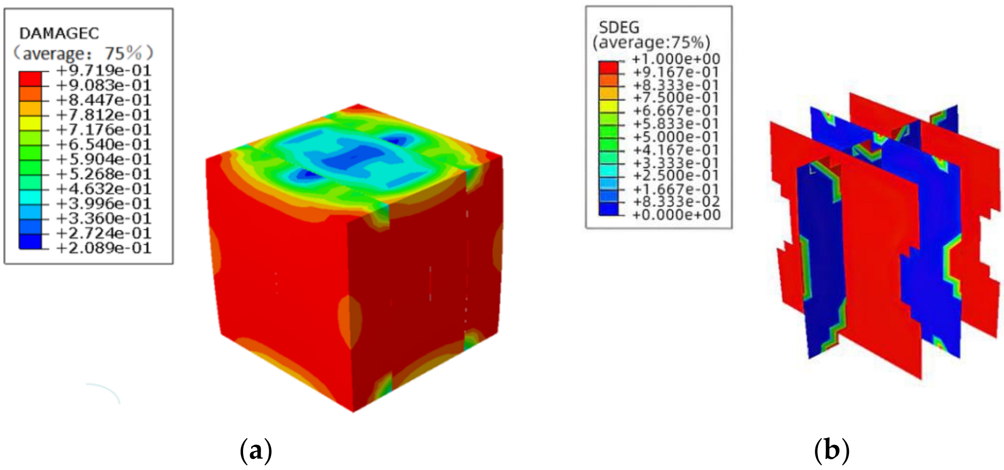

Figure 15. Damage cloud maps of specimen subjected to X-axis loading compression. (**a**) Concrete compression damage; (**b**) Adhesive unit damage.

Figure 16 shows that the maximum stress value of the specimen subjected to axial compression is 56.33 MPa, and that the stress values at the upper and lower edges of the specimen and at the vertical adhesive layer are large. During the experimental test, concrete breaks and falls off, and vertical cracks appear on the two adhesive layers at the edge, which is consistent with the simulation results. The load–displacement curve of the output reference point fit well with the test results, as shown in Figure 17.

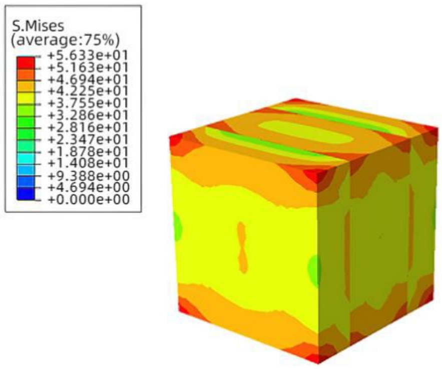

Figure 16. Stress cloud diagram of specimen subjected to X-axis loaded compression.

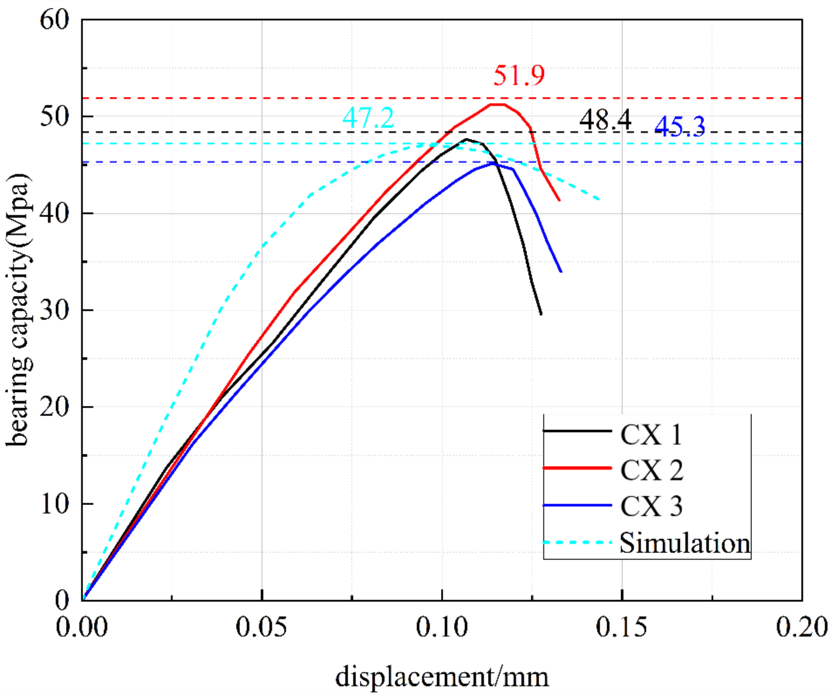

Figure 17. Load–displacement curves associated with the X-axis compression test and corresponding numerical simulation.

Experimental and simulated results have been summarized in Table 21.

Table 21. Comparative analysis of X-axial compression testing and numerical simulation.

Specimen Number	Strength (MPa) Test Values	Strength (MPa) Experimental Average	Simulated Intensity (MPa)	Difference between the Experimental and Simulated Value (%)
CX1	48.4			
CX2	51.9	48.5	47.2	102.8%
CX3	45.3			

Table 21 shows that the experimental value is greater than the simulated value by 102.8%. Compared with the Z-axis loading test, the X-direction loading test has cracks, but the bonding between the layers is better due to the addition of glass fiber, and the fixation test value should be greater than the simulated value. According to the division between finite element units, the compression test in the X-axis direction is compressed by 8 bonded concrete bars, so the simulation value should be greater than that of the Z-axis simulation, which is consistent with the measured data and simulated data.

4.2.3. Y-Axis Compression Simulation

Similarly, cloud maps depicting concrete compression damage, bonding unit damage, and Mises stress caused by Y-axis loading are shown in Figures 18 and 19.

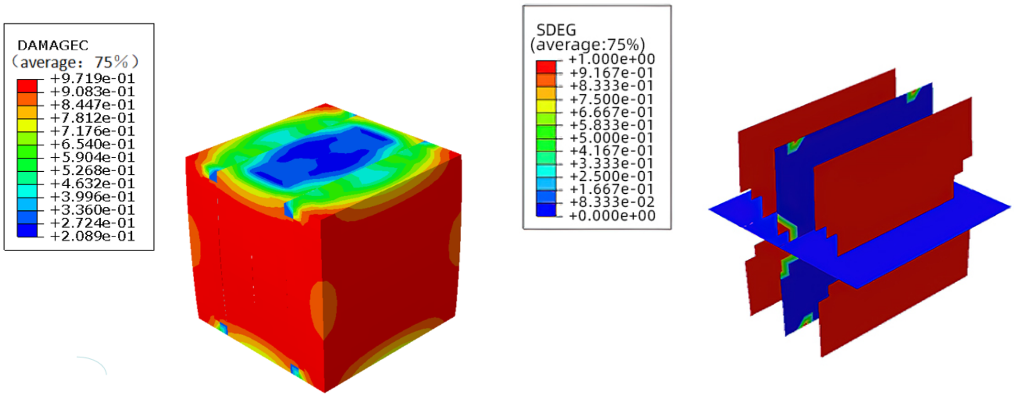

(**a**) (**b**)

Figure 18. Damage cloud maps of specimen subjected to Y-axis loading compression. (**a**) Concrete compression damage; (**b**) Adhesive unit damage.

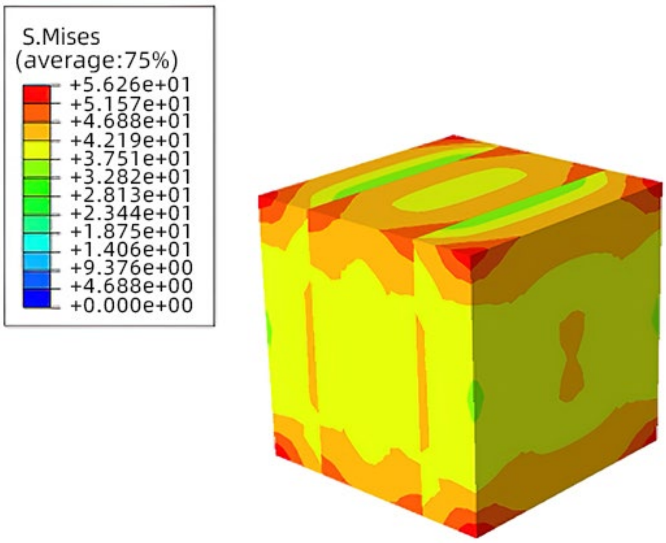

Figure 19. Stress cloud diagram of the specimen subjected to Y-axis loaded compression.

Figure 18 shows that the simulation results of Y-axis loading compression are similar to those of the X-axis loading compression. The compression damage of the two concrete layers at the edge is the largest, and vertical cracks are generated in the bonding layer on both sides of the specimen. The bonding layer on both sides of the specimen is completely damaged, which is consistent with the simulation results.

Figure 19 shows that the maximum stress value of the specimen subjected to axial compression is 56.26 MPa. The stress values at the upper and lower edges of the specimen and at the vertical bonding layer are relatively large, which is consistent with the simulation results. The load–displacement curve of the reference point shows a good fit with that of the test data, as shown in Figure 20.

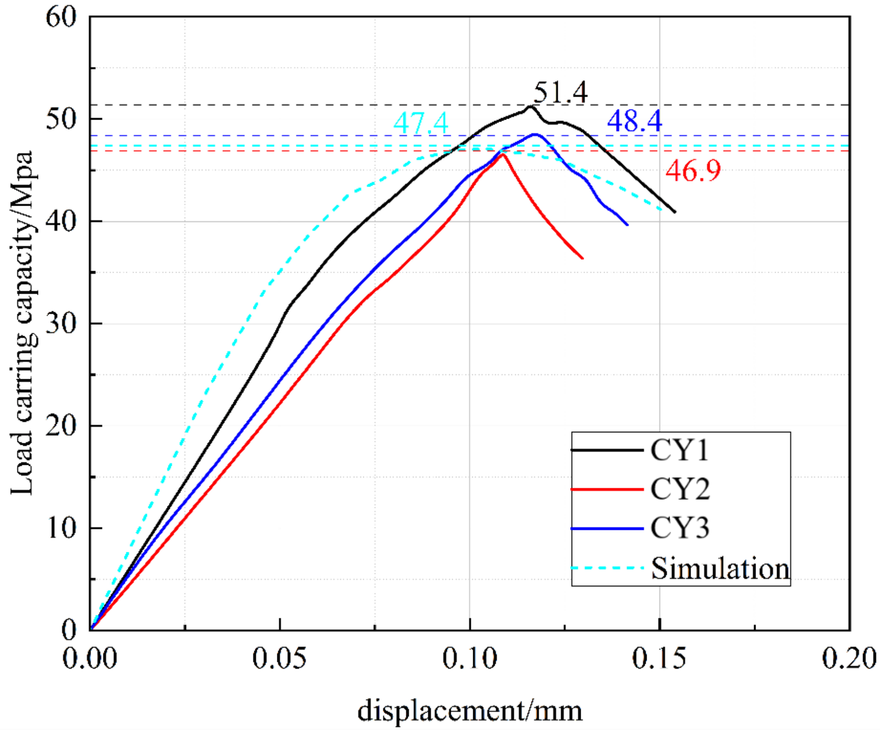

Figure 20. Load–displacement curves associated with the Y-axis compression test and corresponding numerical simulation.

The experimental and simulation results are summarized in Table 22.

Table 22. Comparative analysis of Y-axial compression testing and numerical simulation.

Specimen Number	Strength (MPa) Test Values	Experimental Average	Simulated Value (MPa)	Difference between the Experimental and Simulated Value (%)
CY1	51.4	48.9	47.1	103.8%
CY2	46.9			
CY3	48.4			

Table 22 shows that the experimental mean is greater than the simulated values, or 103.8% of the simulated values.

Compared to the compression test of the Z-axis, the result of the Y-axis compression test is larger than the simulated value, which may be due to the result of horizontal printing. The test value is from large to small, respectively. X > Y > Z, but the simulation results are Y > X > Z. According to the division of the finite element units, the Y-axis test, as it is the whole concrete strip, should be the largest value in the test, which is the same as the simulation results. However, from the perspective of the test data, the big difference between the test groups, this may be because the maintenance is not strictly accurate to 18–22 °C, humidity cannot strictly guarantee above 95%, and cutting blocks cannot avoid the bond between layer and layer, the solid test has particularity, this test is only applicable to the corresponding situation in this paper. Compared with other materials printing, such as 3D metal printing, 3D concrete printing accuracy is poor, and the size between the test blocks is also a certain difference, which also has a certain impact on the final result and cannot guarantee that it is an ideal situation. In the simulation results of the three directions, the error does not exceed 4%, and some partly reflects the mechanical properties. In conclusion, it is feasible to simulate the stress performance of concrete with similar strength, such as C55 concrete.

5. Conclusions

This study presents the preparation procedures and mechanical properties of extruded and cured 3D printed concrete materials The optimized mix design is valid only for the used materials, and the following conclusions were drawn based on the results obtained:

1. Different additives and their contents have varying effects on the strength of concrete. On one hand, excessive additive content causes extremely fast concrete setting, while blocking the 3D printer nozzle. On the other hand, moderate additive may have no impact on the concrete performance. Therefore, it is very necessary to choose appropriate additives.
2. Through a single-factor experiment, an orthogonal test, and fiber optimization of 3D printed concrete, the most optimum mix ratio is determined in this study (3D printed concrete: cement: fly ash: CH powder: water reducing agent: sodium gluconate: latex powder: concrete foaming mass ratio = 0.29:1:0.6:0.2:0.2:0.002:0.0023:0.02:0.002), wherein the glass fiber volume is 0.3%.
3. Twenty-one 3D printed concrete specimens and nine poured concrete specimens are subjected to axial pull-out, axial compression, and three-point bending tests. The mechanical strength of all 3D printed samples is less than that of the poured concrete specimens. Moreover, bending and compression strengths revealed that 3D printing via compression is more efficient. The bonding strength of the 3D printed concrete can be further optimized by mixing the properties of other fibers.
4. In the pulled simulations, numerically simulated data of 3D printed concrete fit the experimentally obtained data of concrete, thereby verifying the feasibility of using cohesion to simulate the bonding performance of 3D printed concrete. The simulated tension strength of the horizontally and vertically printed structures is 1.35 MPa and 1.48 MPa, respectively. The error is within the acceptable range.
5. In the simulation of the compression part, because there are big differences between 3D printing concrete blocks, so the data does not apply to the finite element model, compared with the error of the optimal value of the concrete, and the similar strength of C55 concrete to a certain extent correctly reflects the change trend of 3D printing concrete, and the difference between different axes.
6. The preparation of 3D printed concrete materials is a complex process. There are many other admixtures and mineral admixtures that can affect the properties of printed materials. Therefore, determining the impact of other varieties of admixtures and mineral admixtures on the properties of printing materials requires further exploration; the proposed optimized mixture is valid only for the used materials. Meanwhile, the proposed test method is also not perfect; however, it can be improved in future studies.

Author Contributions: Conceptualization, S.W. and Y.S.; methodology, L.L.; software, T.X.; validation, Y.S. and S.W.; formal analysis, J.Y.; investigation, S.W.; resources, L.L.; data curation, Y.S.; writing—original draft preparation, Y.S.; writing—review and editing, Y.S.; visualization, T.X.; supervision, T.X.; project administration, L.L.; funding acquisition, J.Y. All authors have read and agreed to the published version of the manuscript.

Funding: This research was funded by [Heilongjiang Province Key R & D plan guidance project: Tengyi Health City Key project of Excellence and Key technology R & D] grant number [GZ20210046] And The APC was funded by [Harbin Institute of Technology].

Institutional Review Board Statement: Not applicable.

Informed Consent Statement: Not applicable.

Data Availability Statement: Data used to support the findings of this study is also included in this article.

Acknowledgments: The authors are very grateful to the editors and all anonymous reviewers for their insightful comments.

Conflicts of Interest: The authors declare that there are no conflict of interest.

References

1. Joh, C.; Lee, J.; Bui, T.; Park, J.; Yang, I.-H. Buildability and Mechanical Properties of 3D Printed Concrete. *Materials* **2020**, *13*, 4919. [CrossRef]
2. Wang, B.; Yao, X.; Yang, M.; Zhang, R.; Huang, J.; Wang, X.; Dong, Z.; Zhao, H. Mechanical Performance of 3D Printed Concrete in Steam Curing Conditions. *Materials* **2022**, *15*, 2864. [CrossRef]
3. Lee, J.H.; Kim, J.H. Matric suction and its effect on the shape stability of 3D printed concrete. *Cem. Concr. Res.* **2022**, *159*, 106864. [CrossRef]
4. Panda, B.; Mohamed, N.A.N.; Paul, S.C.; Singh, G.B.; Tan, M.J.; Šavija, B. The Effect of Material Fresh Properties and Process Parameters on Buildability and Interlayer Adhesion of 3D Printed Concrete. *Materials* **2019**, *12*, 2149. [CrossRef]
5. Le, T.T.; Austin, S.A.; Lim, S.; Buswell, R.A.; Gibb, A.G.F.; Thorpe, T. Mix design and fresh properties for high-performance printing concrete. *Mater. Struct.* **2012**, *45*, 1221–1232. [CrossRef]
6. Panda, B.; Ruan, S.; Unluer, C.; Tan, M.J. Improving the 3D printability of high volume fly ash mixtures via the use of nano attapulgite clay. *Compos. Part B Eng.* **2019**, *165*, 75–83. [CrossRef]
7. Ramana, P.V.; Surendranath, A. Assessment of endurance and microstructural properties effect on polypropylene concrete. *Mater. Today Proc.* **2022**, *52*, 2184–2191. [CrossRef]
8. Paul, S.C.; Tay, Y.W.D.; Panda, B.; Tan, M.J. Fresh and hardened properties of 3D printable cementitious materials for building and construction. *Arch. Civ. Mech. Eng.* **2018**, *18*, 311–319. [CrossRef]
9. Wu, Y.-C.; Li, M. Effects of Early-Age rheology and printing time interval on Late-Age fracture characteristics of 3D printed concrete. *Constr. Build. Mater.* **2022**, *351*, 128559. [CrossRef]
10. Korol, E.A.; Tho, V.D. Bond strength between concrete layers of three-layer concrete structures. *IOP Conf. Ser. Mater. Sci. Eng.* **2020**, *775*, 012115. [CrossRef]
11. Feng, P.; Meng, X.; Chen, J.-F.; Ye, L. Mechanical properties of structures 3D printed with cementitious powders. *Constr. Build. Mater.* **2015**, *93*, 486–497. [CrossRef]
12. Li, Y. 3D mechanical hyisotropy and damage mechanism of concrete. *Highw. Traffic Technol.* **2021**, *38*, 81–89. (In Chinese)
13. Fan, J.; Wang, Z.; Li, G. Preparation, Properties and Microstructure of Non-Calcination Rock Powder Brick with Orthogonal Experiments. *Appl. Sci.* **2021**, *11*, 10274. [CrossRef]
14. Hansen, B.S.; Carey, A.S.; Howard, I.L. Effects of Aggregate Shape and Mineralogy on Relationships between Concrete Mechanical Properties. *ACI Mater. J.* **2021**, *118*, 116–125. [CrossRef]
15. Xiao, J.; Long, X.; Qu, W.; Li, L.; Jiang, H.; Zhong, Z. Influence of sulfuric acid corrosion on concrete stress–strain relationship under uniaxial compression. *Measurement* **2022**, *187*, 110318. [CrossRef]
16. Zhao, L.; Zheng, L.; Qin, H.; Geng, T.; Tan, Y.; Zhang, Z. Research on Failure Characteristics of Concrete Three-Point Bending Beams with Preexisting Cracks in Different Positions Based on Numerical Simulation. *Geofluids* **2021**, *2021*, 7892312. [CrossRef]
17. Chen, J.P. Mix Ratio Design and Performance Optimization of Vitrified Microsphere Insulating Mor-Tar. *Adv. Mater. Res.* **2012**, *1672*, 476–478. [CrossRef]
18. Lim, J.H.; Zhang, X.; Ting, G.H.A.; Pham, Q.-C. Stress-cognizant 3D printing of free-form concrete structures. *J. Build. Eng.* **2021**, *39*, 102221. [CrossRef]
19. Cao, X.; Yu, S.; Cui, H.; Li, Z. 3D Printing Devices and Reinforcing Techniques for Extruded Cement-Based Materials: A Review. *Buildings* **2022**, *12*, 453. [CrossRef]
20. Ma, G.; Li, Z.; Li, W. Printable properties of cementitious material containing copper tailings for extrusion based 3D printing. *Constr. Build. Mater.* **2018**, *162*, 613–627. [CrossRef]
21. Ramachandran, D.; George, R.P.; Vishwakarma, V.; Mudali, U.K. Strength and durability studies of fly ash concrete in sea water environments compared with normal and superplasticizer concrete. *KSCE J. Civ. Eng.* **2017**, *21*, 1282–1290. [CrossRef]
22. Liu, R.; Fang, B.; Zhang, G.; Guo, J.; Yang, Y. Investigation of sodium alginate as a candidate retarder of magnesium phosphate cement: Hydration properties and its retarding mechanism. *Ceram. Int.* **2022**, *48*, 30846–30852. [CrossRef]
23. Lesovik, V.; Tolstoy, A.; Fediuk, R.; Amran, M.; Ali, M.; de Azevedo, A.R.G. Improving the Performances of a Mortar for 3D Printing by Mineral Modifiers. *Buildings* **2022**, *12*, 1181. [CrossRef]
24. Nguyen, T.T.N.; Nguyen, A.T.; Vu, Q.V.; Ngo, V.T.; Lam, T.Q.K. The strength of fly ash concrete of experimental design. *Mag. Civ. Eng. None* **2022**, *109*, 10911. [CrossRef]
25. Elmoaty, A.E.M.A.; Morsy, A.M.; Harraz, A.B. Effect of Fiber Type and Volume Fraction on Fiber Reinforced Concrete and Engineered Cementitious Composite Mechanical Properties. *Buildings* **2022**, *12*, 2108. [CrossRef]
26. Subandi, S.; Yatnikasari, S.; Damaiyanti, M.; Azzahra, R.; Vebrian, V. Effect of Additional Fiberglass Fiber on Concrete Performance. *Ann. Chim. Sci. Matér.* **2019**, *43*, 287–292. [CrossRef]
27. Karaaslan, C.; Yener, E.; Bağatur, T.; Polat, R.; Gül, R.; Alma, M.H. Synergic effect of fly ash and calcium aluminate cement on the properties of pumice-based geopolymer mortar. *Constr. Build. Mater.* **2022**, *345*, 128397. [CrossRef]
28. Tikkanen, J.; Penttala, V.; Cwirzen, A. Mineral powder concrete—Effects of powder content on concrete properties. *Mag. Concr. Res.* **2011**, *63*, 893–903. [CrossRef]
29. Zheng, Z.; Zeng, C.; Tian, C.; Wei, X. Mesoscale numerical investigation on the size effect of concrete uniaxial compressive strength under different contact friction. *Constr. Build. Mater.* **2022**, *346*, 128416. [CrossRef]

30. Cong, M.; Zhang, S.; Sun, D.; Zhou, K. Optimization of Preparation of Foamed Concrete Based on Orthogonal Experiment and Range Analysis. *Front. Mater.* **2021**, *8*, 778173. [CrossRef]
31. Ramyar, E.; Cusatis, G. Discrete Fresh Concrete Model for Simulation of Ordinary, Self-Consolidating, and Printable Concrete Flow. *J. Eng. Mech.* **2022**, *148*, 04021142. [CrossRef]
32. Kurnavina, S.O.; Antonov, M.D. The field of cracks directions in reinforced concrete bending elements strengthened by the external composite reinforcement. *Build. Reconstr.* **2020**, 3–13. [CrossRef]
33. Zou, S.; Xiao, J.; Ding, T.; Duan, Z.; Zhang, Q. Printability and advantages of 3D printing mortar with 100% recycled sand. *Constr. Build. Mater.* **2020**, *273*, 121699. [CrossRef]
34. Ye, G.B.; Zhang, Z.; Xing, H.F.; Huang, M.S.; Xu, C. Consolidation of a composite foundation with soil–cement columns and prefabricated vertical drains. *Bull. Eng. Geol. Environ.* **2011**, *71*, 87–98. [CrossRef]
35. Mahmood, W.; Mohammed, A.S.; Asteris, P.G.; Kurda, R.; Armaghani, D.J. Modeling Flexural and Compressive Strengths Behaviour of Cement-Grouted Sands Modified with Water Reducer Polymer. *Appl. Sci.* **2022**, *12*, 1016. [CrossRef]
36. Jiang, B.; Xia, W.; Wu, T.; Liang, J. The optimum proportion of hygroscopic properties of modified soil composites based on orthogonal test method. *J. Clean. Prod.* **2021**, *278*, 123828. [CrossRef]
37. Hao, L.; Xiao, J.; Sun, J.; Xia, B.; Cao, W. Thermal conductivity of 3D printed concrete with recycled fine aggregate composite phase change materials. *J. Clean. Prod.* **2022**, *364*, 132598. [CrossRef]
38. Liu, Y.; Schindler, A.K. Finite-Element Modeling of Early-Age Concrete Stress Development. *J. Mater. Civ. Eng.* **2020**, *32*, 04019338. [CrossRef]
39. Tudjono, S.; Lie, H.A.; As'ad, S. Reinforced Concrete Finite Element Modeling based on the Discrete Crack Approach. *Civ. Eng. Dimens.* **2016**, *18*, 72–77. [CrossRef]